Formation and properties of spatially inhomogeneous plasma density gratings

G. Lehmann * and K. H. Spatschek
Institut für Theoretische Physik I, Heinrich-Heine-Universität Düsseldorf, D-40225 Düsseldorf, Germany

(Received 3 August 2023; accepted 4 October 2023; published 6 November 2023)

Volume plasma density gratings receive increasing interest since, compared to solid-state optical media, they posses significantly higher damage thresholds. The gratings are produced by counterpropagating laser pulses in underdense plasma. When analyzing their optical properties, usually they are assumed to be homogeneous in space. The latter assumption, however, breaks down, especially when the gratings are produced by short high-power laser pump pulses. Then, generically the plasma grating posses an inhomogeneous envelope which results from the superposition of the pump pulses envelopes. The present paper discusses the effect of grating inhomogeneity on reflection and transmission of probe pulses. A Gaussian plasma density grating becomes an apodized grating which offers significant improvement over homogeneous gratings due to side-lobe suppression while maintaining reflectivity and a narrow bandwidth. On the other hand, the reflected probe pulses receive a chirp which depends on the spatial scale. For a Gaussian grating a cubic spectral phase appears. Numerical particle-in-cell simulations are supported by theoretical analysis based on coupled mode equations as well as an effective medium approach.

DOI: 10.1103/PhysRevE.108.055204

I. INTRODUCTION

Nature has used photonic structures with periodically varying optical properties for about 500 million years to control light [1]. Photonic effects are responsible for broadband light reflectance in almost all biological systems [2]. The periodicity in photonic structures leads to optical bands that are analogous to the electronic bands in semiconductor physics [3]. Spectroscopy based on photonic structures like diffraction gratings inspired significantly modern science. Increasing understanding of the possibilities to manipulate the flow of light stimulated several technological revolutions in signal processing, communications, computing, physics, astrophysics, biology, and even medicine [1].

With the invention of the laser, decades ago a new radiation source entered the scene which enlarged the possible applications and opened completely new fields like fiber optics and laser spectroscopy. Since then the demand for high-power laser systems increased continuously. To avoid damage of optical components in high-power laser systems, a technique called chirped pulse amplification was introduced [4]. Initially, pulse. stretching and compression were performed almost exclusively by pairs of surface diffraction gratings [5]. The highest peak power follows from the optical threshold of the compressor components. Compared to solid-state materials, plasma—being already ionized—does not suffer from breakdown at extreme light intensities. Therefore, now more and more plasma-based optical components come into the center of interest.

Malkin and Fisch [6] were among the first authors who proposed techniques to manipulate ultraintense laser pulses in plasmas. Meanwhile, several groups developed the field of high-intensity plasma photonics. Among them are those of Refs. [7–10], to mention only some of them. Manipulating light using plasmas became a growing field. Plasma parametric amplification [11–16] is part of the newly developing domain of plasma optics, which eventually will pave the way to high-intensity lasers [17–19]. During the past few years plasma mirrors [20], wave- and q-plates [21,22], as well as plasma-based polarizers [23–25] have showed already their enormous potential as high-intensity photonic devices. Plasma optical modulators [26], active plasma lenses [27–30], plasma holograms [31–34], terahertz radiation sources [35], as well as plasma-based beam combiners for very high fluence and energy [36] are under active consideration.

Plasma gratings [37–39], also called plasma photonic crystals [40–43], often represent the underlying structures for novel optical components. A plasma photonic crystal can be understood as a periodic modulation of the refraction index, with the period close to half the wavelength of light [44]. It should be emphasized that once the basic realization in plasma was clarified, many of the intriguing phenomena could be uncovered in analogy to the well-established results for optical crystals [45,46]. The formation of deep electron and ion density gratings by the interaction of two counterpropagating laser pulses was studied already at the beginning of the century [37,47]. Since then, many fundamental properties have been worked out [20,25,26,33,48–58].

The plasma photonic crystal itself has evolved into a promising optical component being more or less ready for applications [59–67]. The plasma grating is tunable since its period can be varied when changing the angle between the pump pulses. For high-power lasers, the production of

*Author to whom correspondence should be addressed: goetz@tp1.uni-duesseldorf.de

chirped plasma gratings [68] is a major challenge for the future. Chirped gratings may be produced by the interference of a convergent laser pulse with a divergent one [5,69–76]. At present still another aspect is in the focus, namely spatial inhomogeneity. A plasma does not allow to manufacture a grating with sharp boundaries and quite homogeneous amplitude. Typically, a grating is produced by intersecting pump laser pulses. Their profiles determine the spatial envelope of the produced grating. Thereby, grating structures with constant grating periods but space-dependent envelopes appear [68,77–79]. A strictly homogeneous plasma grating with constant amplitude is an idealization whose limits should be disclosed. This is the purpose of the present paper.

Particle-in-cell (PIC) simulations are, from the numerical point of view, particularly suitable for revealing the advantages and limitations of plasma gratings. But also several analytical techniques, like optical wave mixing and coupled mode approach [80,81], are available. The theoretical toolbox is complemented by an effective medium approach [5,78,82,83] which can be further refined for a plasma grating. In comparison to a purely homogeneous grating, we aim to investigate the advantages and disadvantages of spatial inhomogeneities. Our focus lies on reflected pulses, as they are typically used in compressors. Stimulated by the diverse research on optical pulses in solid-state lattices and other dielectric elements [45,46], we also anticipate significant effects of the plasma structure on the reflection and transmission properties.

The basis of our investigations relies on PIC simulations. In order to better understand the fundamental phenomena observed in these simulations, we employ simple analytical models for interpretation.

The plan of the paper is as follows. We start with PIC simulations of inhomogeneous gratings in Sec. II. The grating structure is analyzed for two pump pulses in head-on collision. Due to the ponderomotive force, first a lattice appears on the electron timescale. Later, the ions follow the space charge field created by the nonuniformly distributed electrons, building a transient plasma grating. The form of the latter is interpreted by a simple fluid model. Next, in Sec. III, we investigate the behavior of a probe pulse interacting with the plasma grating. Transmission and reflection are reported. The main focus of our investigation lies on the advantages of less sharp grating edges (apodization) as well as on the phase effects (chirp) caused by the inhomogeneity. The dynamics of the probe pulses is first analyzed by coupled mode equations. In Appendix we supplement the coupled mode analysis by an effective medium approach. The latter is quantified through a Wentzel-Kramers-Brillouin (WKB) analysis. The paper is concluded by a conclusion and outlook.

II. INHOMOGENEOUS PLASMA DENSITY GRATING EVOLUTION

A. Simulation results

To demonstrate the formation and discuss the properties of inhomogeneous plasma density gratings, let us begin with results from one-dimensional PIC simulations using the EPOCH code [84]. In the center of our simulation box we have

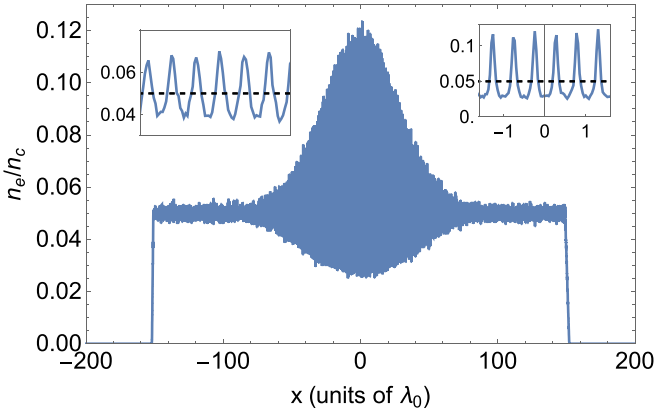

FIG. 1. Inhomogeneous plasma density grating at $t = 1.5$ ps after the overlap of the 300 fs driving pump pulses of intensity 10^{15} W/cm^2. The initial unperturbed plasma density $n_0 = 0.05n_c$ is shown as dashed line in the two insets. The resulting spatial inhomogeniety of the modulation amplitude is apparent.

a slab of almost homogeneous hydrogen plasma with initial density $n_0 = 0.05n_c$, where n_c is the critical density following from $\omega_0 = \sqrt{4\pi n_c e^2/m_e}$, and ω_0 is the laser frequency. To the left and right of the plasma slab we have vacuum of sufficient lengths to follow laser pulses leaving the plasma in either direction. From both ends of the box, we simultaneously launch pump pulses of wavelength $\lambda_0 = 800$ nm and Gaussian temporal profiles with full width at half maximum duration of 300 fs (of the electric field). The peak intensity of the pulses is 10^{15} W/cm^2. The spatial extent of the overlap region of the two pulses is about 100 λ_0, the length of the plasma slab is 300 λ_0. Thus, the full pulse overlap region is contained in the plasma, which is different from several previous studies. The electron plasma temperature has been set to $T_e = 2.5$ eV and ion temperature to $T_i = T_e/10$. We define $t = 0$ as the time at which the maxima of the two laser pulses coincide in the center of the plasma at $x = 0$. The simulation box is 1500 λ_0 long and uses 26 cells per λ_0. Per cell occupied by plasma we have 200 macroparticles per species. The ion to electron mass ratio is 1836, and the plasma is assumed preionized.

Once the laser pulses overlap, the ponderomotive force due to the beat of the two laser pulses starts driving electron density modulations with a spatial period of $\lambda_1/2$, where $\lambda_1 = \lambda_0/N_0$ is the laser wavelength inside the plasma and $N_0 = \sqrt{1 - n_0/n_c}$.

Figure 1 shows the electron plasma density at $t = 1.5$ ps. The ion density at this time is almost identical to the electron density, i.e., the structure is almost quasineutral. Due to the temporal intensity profiles of the pump pulses, the ponderomotive beat acquires a spatiotemporal dependence, which is then subsequently imprinted into amplitude of the plasma density modulation (see Sec. II B). The insets in Fig. 1 show that the anharmonicity of the modulation is clearly different at various locations inside the grating, whereas the period is the same everywhere. In the wings, where the amplitude of the grating is small, the modulation is almost harmonic and close to symmetric about the unperturbed initial density. In the center of the grating, the modulation amplitude is larger and the anharmonicity is substantial. The thin density spikes

reach up to $2.5n_0$, whereas the troughs have a density of approximately $0.5n_0$.

A spatially more homogeneous grating has been achieved in previous studies by shortening the plasma, such that the plasma is much shorter than the overlap region of the two pump pulses (i.e., only the center of the grating has been considered). Then the density modulation has close to uniform amplitude. The very thin underdense plasma slab, however, is experimentally at least challenging to realize. Here we investigate the experimentally more realistic situation, where the plasma is longer than the overlap region of the laser pulses, resulting in the variation of the grating amplitude. As we will show in the subsequent sections, this variation affects the reflective properties of the plasma gratings.

B. Fluid model for plasma density grating evolution

Now we discuss a simple analytic model which explains the main findings of the previous subsection. Very detailed investigations of the nonlinear dynamics of *homogeneous* laser-generated ion-plasma gratings do exist [41]. For the discussion of *inhomogeneity* we start from a simplified homogeneous model [58]. It turned out that the latter model describes the initial phase of the *homogeneous* situation quite well.

We will normalize frequency ω by the pump frequency ω_0, time t by $2\pi/\omega_0$ (approx. 2.67 fs), distances by the laser wavelength λ_0 in vacuum (800 nm), and wave numbers k by $k_0 \equiv 2\pi/\lambda_0$. In plasma, the pump wave number is $k_1 = k_0 N_0$. The mean density n_0 will be used for density normalization, while the velocity of light c is the velocity unit. Then $2k_1 x \to 4\pi N_0 x$ in nondimensional form. A laser pulse propagates in plasma with group velocity $v_{g0} = cN_0$. Normalized vector potentials $\vec{a} = \frac{e}{m_e c}\vec{A}$ are being used.

The single pulse pump envelopes are assumed as

$$\text{pump envelope} \sim \exp\left[-\frac{(x \mp x_0 \pm v_{g0}t)^2}{2\langle x^2\rangle}\right], \tag{1}$$

where $\langle x^2\rangle$ designates the mean square width of the pump pulses. Initially, the two counterpropagating pumps are well separated when centered around $\pm x_0$. Overlapping at later times leads to the factor

$$\mathcal{E}_{a_0 a_0} = e^{-\frac{-x^2}{\langle x^2\rangle}}\, e^{-\frac{-v_{g0}^2 t^2}{\langle x^2\rangle}} \tag{2}$$

for the combined action if we reset the zero point of the timeline accordingly. Then the factor $\mathcal{E}_{a_0 a_0}$ appears in the ponderomotive potential during the head-on collision of two oppositely propagating single pump pulses. In the following the variation of the envelopes is assumed as slow on the λ_0 scale. Produced by two pumps with amplitudes a_0, the rapidly varying part of the ponderomotive potential ϕ_p (here still in dimensional form) is [56]

$$\frac{\phi_p}{m_e c^2} \approx -\frac{1}{2} a_0^2 \mathcal{E}_{a_0 a_0} \cos(2k_1 x - \varphi), \tag{3}$$

where φ is a phase mismatch. Space charge effects create an averaged electric field

$$\langle E_x\rangle \approx -4\pi e n_0 \frac{\omega_{b0}^2}{2k_1 \omega_{pe}^2} \mathcal{E}_{a_0 a_0} \sin(2k_1 x + \varphi), \tag{4}$$

where we introduced the electron bounce frequency $\omega_{b0} = \sqrt{2} a_0 \omega_0$. Following Ma *et al.* [58] we may determine a fluid velocity u_i of ions from [56,58]

$$m_i \frac{\partial u_i}{\partial t} \approx Ze\langle E_x\rangle. \tag{5}$$

We set $Z = 1$. The nondimensional formulation, using the units mentioned above and introducing

$$b = 2\pi a_0^2 N_0^{-1} \frac{m_e}{m_i}, \quad h = 4\pi N_0, \tag{6}$$

follows as

$$\frac{\partial u_i}{\partial t} = -b\, e^{-N_0^2 t^2/\langle x^2\rangle} \sin(hx)\, e^{-x^2/\langle x^2\rangle}. \tag{7}$$

Actually, the pumps are highly active as long as $t \lesssim \sqrt{\langle x^2\rangle}/N_0$. However, since we are interested in the ion reaction at larger timescales, approximately on the order of $t \sim \mathcal{O}(\sqrt{\frac{m_i}{m_e}\frac{n_c}{n_0}})$, we may make the simplified assumption that the ion velocity remains constant at later times, at least in the simplest approximation. Then, using $\int_{-\infty}^{\infty} e^{-N_0^2 t^2/\langle x^2\rangle} dt = \frac{\sqrt{\pi\langle x^2\rangle}}{N_0}$, the zeroth-order result,

$$u_i^{(0)} \approx -b_0 \sin(hx)\, e^{-x^2/\langle x^2\rangle}, \quad b_0 = 2\pi\sqrt{\pi} a_0^2 \sqrt{\langle x^2\rangle} N_0^{-2} \frac{m_e}{m_i}, \tag{8}$$

will follow. However, a more accurate calculation is possible starting from

$$u_i = -b \sin(hx)\, e^{-x^2/\langle x^2\rangle} \int_{-\infty}^{t} e^{-N_0^2 t'^2/\langle x^2\rangle} dt'. \tag{9}$$

We let ourselves be guided by the formulation of Ma *et al.* [58] for the density continuity equation,

$$\frac{\partial n}{\partial t} + u_i \frac{\partial n}{\partial x} = -n \frac{\partial u_i}{\partial t}. \tag{10}$$

Note that with respect to $\sin(hx)$ and $\cos(hx)$ the exponential function $e^{-x^2/\langle x^2\rangle}$ is slowly varying in space. We shall make use of this fact when determining an approximate solution of the initial value problem. We also introduce a new time τ via

$$d\tau = dt \int_{-\infty}^{t} e^{-N_0^2 t'^2/\langle x^2\rangle} dt', \tag{11}$$

such that

$$\tau = \int_0^t dt'' \int_{-\infty}^{t''} e^{-N_0^2 t'^2/\langle x^2\rangle} dt' \tag{12}$$

for $t \geqslant 0$, leading to

$$\tau(t) = \frac{\sqrt{\pi\langle x^2\rangle}}{2N_0} t \left[1 + \operatorname{erf}\left(\frac{N_0 t}{\sqrt{\langle x^2\rangle}}\right)\right] + \frac{\langle x^2\rangle}{2N_0^2}[e^{-N_0^2 t^2/\langle x^2\rangle} - 1]. \tag{13}$$

Written in detail with respect to time τ, the approximate equation for ion continuity is given by

$$\frac{\partial n}{\partial \tau} - b \sin(hx)\, e^{-x^2/\langle x^2\rangle} \frac{\partial n}{\partial x} \approx b\, h \cos(hx)\, e^{-x^2/\langle x^2\rangle} n. \tag{14}$$

To eliminate the coefficients h and b, we modify in the present subsection the already nondimensional variables t and x to

$$\tilde{t} = hb\,\tau, \quad \tilde{x} = hx, \tag{15}$$

obtaining

$$\frac{\partial n}{\partial \tilde{t}} - \tilde{\mathcal{E}}\,\sin(\tilde{x})\,\frac{\partial n}{\partial \tilde{x}} \approx \tilde{\mathcal{E}}\,\cos(\tilde{x})\,n, \tag{16}$$

with

$$\tilde{\mathcal{E}} = e^{-\frac{\tilde{x}^2}{\langle \tilde{x}^2\rangle}}, \quad \langle \tilde{x}^2\rangle = h^2\langle x^2\rangle. \tag{17}$$

Next, we should familiarize ourselves with the following intuitive picture. We have already assumed that the envelope is slowly varying in space. That means we may introduce a local (space-dependent) time T (and for aesthetic reasons also $X \equiv \tilde{x}$), i.e.,

$$T = \tilde{t}e^{-\frac{\tilde{x}^2}{\langle \tilde{x}^2\rangle}}, \quad X \equiv \tilde{x}. \tag{18}$$

This *local* time reflects the fact that pulses effectively interact for different durations at different locations. The basic equation now becomes

$$\frac{\partial n}{\partial T} - \sin(X)\,\frac{\partial n}{\partial X} = \cos(X)\,n. \tag{19}$$

We have replaced the approximate sign with an equality sign, fully aware that we are only seeking an approximate solution. As long as we do not care about the initial condition, the solution of this quasilinear differential equation can be written with an arbitrary function F as

$$n(X,T) = \frac{F\{-\ln[\csc(X)+\cot(X)]+T\}}{\sin(X)}. \tag{20}$$

At time $T = 0$, we propose the condition $n(X,0) = 1$. With $z \equiv \sin(X)$ we obtain the relation

$$z = F\left(-\ln\left[\frac{1+\sqrt{1-z^2}}{z}\right]\right) \equiv F(f(z)). \tag{21}$$

Thus, $f(z)$ is the inverse of the function $F(z)$. From

$$f(z) = F^{-1}(z) \quad \text{with} \quad f^{-1}(z) = \frac{2e^z}{(e^z)^2+1} \tag{22}$$

we obtain

$$F(Z) = \frac{2e^Z}{e^{2Z}+1}, \tag{23}$$

leading to the result

$$n(X,T) = \frac{1}{\sin(X)}\,\frac{2e^Z}{e^{2Z}+1}\bigg|_{Z=T-\ln[\csc(X)+\cot(X)]}. \tag{24}$$

From a straightforward evaluation of the right-hand side the final expression

$$n(X,T) = 2e^T\,\frac{1+\cos(X)}{[1+\cos(X)]^2+e^{2T}\sin^2(X)} \tag{25}$$

follows. Remember the definitions (15) and (18) which introduce the inhomogeneous envelope at time t. They lead to

$$n(x,t) = 2e^T\,\frac{1+\cos(X)}{[1+\cos(X)]^2+e^{2T}\sin^2(X)}\bigg|_{X=hx,\,T=hb\,\tau(t)e^{-x^2/\langle x^2\rangle}}. \tag{26}$$

TABLE I. Fourier-coefficients for the lowest-order harmonics of the analytic solution for the plasma density (26) at $t = 560$. Note that all β_m vanish because of even symmetry of the plasma density $n(x,t)$.

m	0	1	2	3	4	5
$\alpha_m(560)$	2.000	0.89	0.40	0.18	0.08	0.03

Before we compare the analytical solution with a numerical one, let us discuss an approximation that will be used to evaluate the simple models presented in the subsequent sections. In these models, we neglect deviations from purely harmonic behavior, meaning we neglect higher harmonics.

Clearly, the result (26) consists of several harmonic contributions $\sim\cos(mhx)$, $m = 1, 2\ldots$ [and perhaps additional odd parity parts $\sim\sin(mhx)$]. To estimate the significance of each Fourier component, we define coefficients that depend on time, namely

$$\alpha_m(t) = \frac{2}{L^*}\int_0^{L^*}\cos(mx)\,n(x,t)\,dx, \tag{27}$$

$$\beta_m(t) = \frac{2}{L^*}\int_0^{L^*}\sin(mx)\,n(x,t)\,dx, \tag{28}$$

where $L^* = 1/2N_0$ is the periodicity of $n(x,t)$ when x is measured in λ_0. These coefficients are borrowed from the homogeneous case, i.e., from $n(x,t)$ for $\langle x^2\rangle \to \infty$. We assess their importance, for example at time $t = 560$ (corresponding to 1.5 ps), from Table I.

Using the Fourier coefficients, we construct the following simple model for the inhomogeneous grating density,

$$n^M_{\text{approx}}(x,t) = \frac{1}{2}\alpha_0(t) + \sum_{m=1}^{M}[\alpha_m(t)\,\cos(mhx) + \beta_m(t)\,\sin(mhx)]\,e^{-x^2/\langle x^2\rangle}. \tag{29}$$

It is found that even for low M Eq. (29) provides an excellent approximation for $n(x,t)$. Equation (29) will be used to evaluate the coupled mode equations and apply the effective medium approach.

For a fixed value of n_0/n_c, as well as given pump amplitudes a_0 and widths $\langle x^2\rangle$, there is still one free parameter, which is time t. Figure 2 shows the density distributions for $n_0/n_c = 0.05$, $a_0 = 0.0216$, and $\langle x^2\rangle = 2300$. The left subfigure shows the analytic solution (26) for $t = 560$, while the right subfigure shows the approximate solution (29) for $M = 3$ at the same time.

Comparing the density obtained from the PIC simulation (Fig. 1) to the result of the analytic model [Fig. 2(a)] we find very good agreement. Modulation amplitude and asymmetry, in terms of maximum and minimum density per period, are very well reproduced. The analytic solution slightly overestimates the amplitude of the density modulation by a few percentages, which is due to the approximation of almost constant ion velocity u_i.

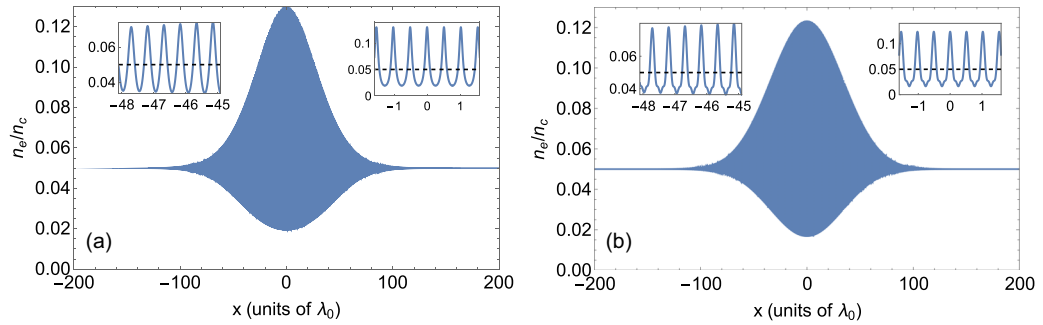

FIG. 2. Plasma grating structures for $n_0 = 0.05n_c$ and $\langle x^2 \rangle = 2300$. (a) The analytic result (26) at $t = 560$. (b) In comparison, the simpler model (29) for $M = 3$. The dashed line in the insets represents the initial density of $0.05n_c$.

III. TRANSMISSION, REFLECTION, AND PHASE OF A PROBE PULSE

The most prominent feature of a plasma density grating is that it may act as a plasma photonic crystal to probe laser pulses. In particular the use of plasma gratings as Bragg-type mirrors for high-intensity laser pulses may be of interest. In case of homogeneous gratings, a linear plane wave ansatz gives insight into the dispersive properties for electromagnetic wave propagation [40,43,46]. In this section we will, at first, demonstrate the reflective properties of inhomogenous gratings via simulations. Subsequently, coupled mode equations are derived to explain these observations. In what follows, the probe is always sufficiently short that the grating dynamics can be neglected, i.e., the probe interacts with an almost stationary grating.

A. Simulation results

In our simulation we consider a linearly polarized 30-fs Gaussian probe pulse with maximum intensity 10^{15} W/cm^2, interacting with the grating shown in Fig. 1. The probe pulse has the same central wavelength (800 nm) as the pulses driving the grating and is launched from the left boundary such that its maximum reaches $x = 0$ at $t = 1.5$ ps. Figure 3(a) shows the electric field of reflected and transmitted parts of this laser pulse after the interaction. As reference and guide for the eye, we also show the original probe pulse and the position of the plasma grating in the simulation box. The electric fields are normalized to the maximum electric field $E_{z,0}$ of the incoming probe pulse.

The structure of the reflected and transmitted pulses is determined by their spectral content and the phase relation between the contained frequencies. The spectrum of incoming, reflected, and transmitted pulses is shown in Fig. 3(b), respectively. Only the central part (about $\frac{1}{4}$) of the incoming spectrum is reflected, and everything else is transmitted. Less than 1% of the probe energy remains in the plasma. The reflected spectrum has almost (super-)Gaussian form; hence, if the reflected pulse was bandwidth limited, then it should have about four times the duration of the incoming pulse. The reflected pulse, however, now has the form of a pulse train and is much longer than four times the initial duration. While interacting with the grating, the spectral components undergo a phase shift, which introduces a quadratic chirp, i.e., the grating has third-order dispersion. The transmitted pulse mainly consists of all the frequencies that are not reflected but also shows features of photon acceleration and deceleration (the two horns at $k \approx k_0 \pm 0.01k_0$). The small surplus of energy at these frequencies, compared to the incoming light, stems from frequency conversion processes [85] affecting some of the light in the band gap.

B. Coupled mode equations for reflection, transmission, and phase

We now analyze the PIC results with the help of coupled mode equations. An alternative method in the form of the

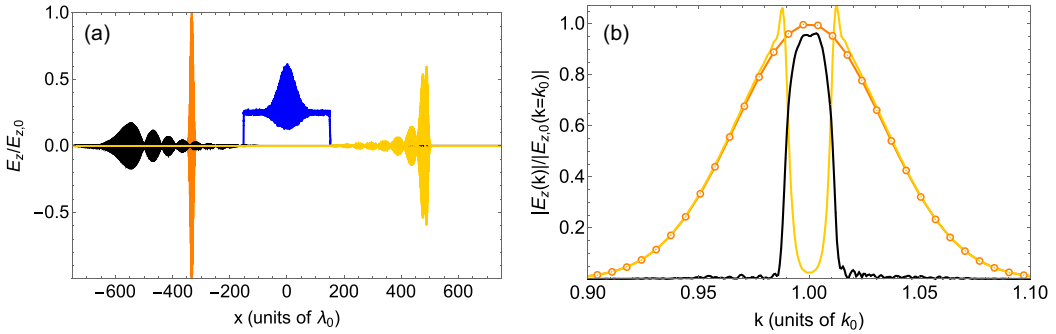

FIG. 3. (a) Interaction of a 30-fs probe pulse (propagating to right) with the inhomogeneous plasma grating (indicated in the box center). Shown are the electric fields of the incoming probe pulse [orange (gray) line] before the interaction, the reflected pulse (black line), and the transmitted pulse [yellow (light gray) line]. (b) Spectrum of incoming (orange circles), reflected (black line), and transmitted [yellow (light gray) line] electric field.

effective medium approach is briefly outlined in the Appendix. First, we set up the equations. Subsequently they will be solved with appropriate boundary conditions to determine the transmission and reflection coefficients as well as the phase of the reflected wave.

We consider a test wave $E \sim e^{-i\omega t}$ with frequency ω such that (before normalization)

$$\frac{d^2E}{dx^2} + k^2\frac{N^2}{N_0^2}E = 0 \tag{30}$$

with

$$k \equiv \frac{\omega N_0}{c}, \quad N = \sqrt{1 - \frac{\omega_{pe}^2}{\omega^2}}. \tag{31}$$

N is the refractive index and N_0 is the reference index. Obviously, when the test wave frequency approaches the pump frequency, i.e., $\omega \to \omega_0$, we have

$$k \to k_1 \equiv \frac{\omega_0 N_0}{c}, \quad N \to N_0 = \sqrt{1 - \frac{\omega_{pe}^2}{\omega_0^2}}. \tag{32}$$

Introducing normalized quantities (as in Sec. II B) and the (normalized) frequency mismatch Δ we find

$$\Delta = \omega - 1 \quad \rightsquigarrow \quad k^2 \approx k_1^2(1 + 2\Delta) \tag{33}$$

for $|\Delta| \ll 1$. Also

$$N^2 \approx N_0^2\left\{1 + \left[1 - \frac{1}{N_0^2}\right]\delta n_e - \left[1 - \frac{1}{N_0^2}\right]2\Delta\right\}, \tag{34}$$

and

$$k^2\frac{N^2}{N_0^2} \approx k_1^2\left(1 + \left[1 - \frac{1}{N_0^2}\right]\delta n_e + \frac{2}{N_0^2}\Delta\right). \tag{35}$$

The electron density variation δn_e is driven by the ponderomotive force and may show the behavior as discussed in Sec. II.

In the following we present results using the approximation (29) with $M = 1$ at time $t = 560$. Then (29) takes on the particularly simple form

$$\delta n_e \approx \tfrac{1}{2}A(x)(e^{i\psi} + e^{-i\psi}), \quad A(x) \approx \alpha_1(t = 560)\, e^{-x^2/\langle x^2\rangle}$$
$$\approx 0.89\, e^{-x^2/\langle x^2\rangle}, \tag{36}$$

for

$$\psi = 2\xi + \varphi(\xi), \quad \xi = \frac{2\pi}{\lambda_1}x, \tag{37}$$

when the (dimensional) quantity $\lambda_1 = \frac{2\pi c}{\omega_0 N_0}$, as well as the (dimensional) space coordinate x, are made dimensionless with respect to $\lambda_0 = \frac{2\pi c}{\omega_0}$. Obviously, $\xi = 2\pi N_0 x = \frac{h}{2}x$. We allow for an additional phase φ. The phase will become important for chirped gratings. In the present case we can set $\varphi = 0$. Then the (normalized) wave equation takes the form

$$\frac{d^2E}{dx^2} + (2\pi N_0)^2\left\{1 + \frac{2}{N_0^2}\Delta + \frac{1}{2}\left[1 - \frac{1}{N_0^2}\right]A(x)\right.$$
$$\left.\times\ (e^{i4\pi N_0 x + i\varphi} + e^{-i4\pi N_0 x - i\varphi})\right\}E = 0. \tag{38}$$

For the electric field E we make the ansatz

$$E(x) = a_+(x)e^{i2\pi N_0 x} + a_-(x)e^{-i2\pi N_0 x}, \tag{39}$$

with slowly varying envelopes $a_\pm$. Below we shall generalize to carrier wave numbers $k \neq k_0$.

Within a slowly varying envelope approximation one obtains for the amplitudes u and v, which are defined through

$$a_+(x) = u(x)e^{i\varphi/2}, \quad a_-(x) = v(x)e^{-i\varphi/2}, \tag{40}$$

the standard coupled mode equations

$$\frac{du(x)}{dx} = i[\sigma(x)\,u(x) + \kappa(x)\,v(x)], \tag{41}$$
$$\frac{dv(x)}{dx} = -i[\sigma(x)\,v(x) + \kappa(x)\,u(x)]. \tag{42}$$

Here

$$\sigma(x) = \frac{2\pi}{N_0}\Delta, \tag{43}$$
$$\kappa(x) = \frac{\pi N_0}{2}\left(1 - \frac{1}{N_0^2}\right)A(x). \tag{44}$$

Now a few remarks concerning boundary conditions and reflection as well as transmission coefficients. Since in nondimensional form

$$2\pi N_0(1 + \Delta)x = 2\pi kx, \tag{45}$$

we may introduce

$$\sigma = 2\pi N_0\Delta + \bar\sigma, \quad \tilde u = u\,e^{-i2\pi N_0\Delta x}, \quad \tilde v = v\,e^{i2\pi N_0\Delta x}, \tag{46}$$

to obtain the test electric field (in nondimensional form) with appropriate carrier wave number k,

$$E = \tilde u(x)\,e^{2\pi ikx} + \tilde v(x)\,e^{-2\pi ikx}. \tag{47}$$

This is the generalization of (39) for $k_0 \to k$. The corresponding modified coupled mode equations are

$$\frac{d\tilde u(x)}{dx} = i[\bar\sigma(x)\,\tilde u(x) + \kappa(x)\,e^{-i4\pi N_0\Delta x}\,\tilde v(x)], \tag{48}$$
$$\frac{d\tilde v(x)}{dx} = -i[\bar\sigma(x)\,\tilde v(x) + \kappa(x)\,e^{i4\pi N_0\Delta x}\,\tilde u(x)] \tag{49}$$

with

$$\bar\sigma(x) = -2\pi N_0\left(1 - \frac{1}{N_0^2}\right)\Delta. \tag{50}$$

When solving the coupled mode equations for a finite grating in the region $-L \leqslant x \leqslant L$ we use the boundary conditions $\tilde u(-L) = 1$ and $\tilde v(L) = 0$. Then the reflection coefficient R and the transmission coefficient T follow (for $\varphi \equiv 0$) via

$$r = v(-L)e^{-i2\pi N_0\Delta L} \to R \equiv |r|^2 = |v(-L)|^2,$$
$$t = u(L)e^{-i2\pi N_0\Delta L} \to T \equiv |t|^2 = |u(L)|^2. \tag{51}$$

The solution of the coupled mode equations is numerically simple. In Fig. 4 we present results for the the transmission coefficient T and the reflection coefficient R, respectively. The coefficients depend on the frequency shift Δ. Figure 4 shows the coefficients for $M = 1$ and $\alpha_1 = 0.89$ with $\langle x^2\rangle = 2300$, assuming a plasma density $n_0/n_c = 0.05$ and $L = 150$.

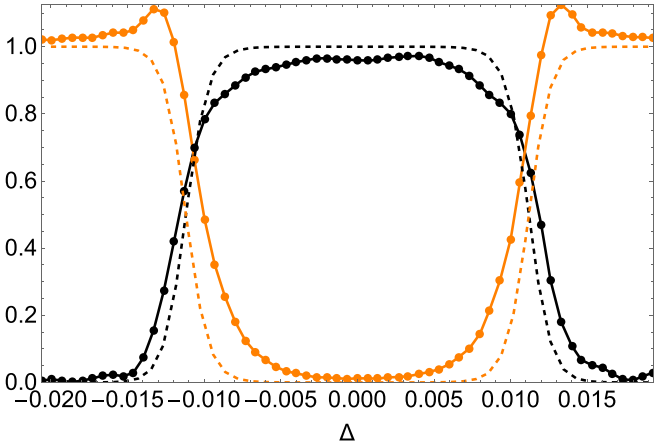

FIG. 4. Solutions of the coupled mode equations for the transmission coefficient T [orange (light gray) dashed line] and the reflection coefficient R (black dashed line) in the region $-0.02 \leqslant \Delta \leqslant 0.02$. The model grating (29) is applied for $M = 1$ and $A(x) = 0.89e^{-x^2/\langle x^2\rangle}$ with $\langle x^2\rangle = 2300$. For the plasma density we have $n_0/n_c = 0.05$ and $L = 150$. Solid lines with symbols are the respective data obtained from a PIC simulation corresponding to Figs. 3(a) and 3(b).

Note that the effective width of the inhomogeneous grating is $\sqrt{\langle x^2\rangle} \approx 48$. Figure 4 additionally shows R and T, respectively, as obtained from from the PIC simulation discussed in Sec. III A. R and T are in this case obtained via the data shown in Fig. 3(b). The reflected and transmitted amplitude is normalized to the amplitude of the incoming spectrum, respectively, for every frequency. Overall, we find a good agreement of the coupled mode results with the PIC simulation results.

Let us now focus on the reflected laser pulse shown in Fig. 3(a). Its temporal profile is not only determined by the spectral content, i.e., the spectrum of the incoming pulse weighted by $R(\Delta)$ but also by the relative phase $\Phi(\Delta) \in [-\pi, \pi)$ of the modes. Instead of taking $\Phi = \arg(r)$, we may directly use $\Phi = \arg(v(-L))$, as the $\exp(-i2\pi N_0 \Delta L)$ factor only adds an additional linear phase variation with Δ, causing only a temporal shift in the time domain. Figure 5 shows the variation of Φ with Δ. For the region where $R(\Delta) > 0$, we fit $\Phi(\Delta)$ with a cubic polynomial $p(\Delta) = 560\Delta + 2.97 \times 10^6 \Delta^3$ and find very good agreement between fit and numerically obtained curve. The cubic contribution to the phase is related to quadratic chirp [86], which is the source for the pulses trailing the main pulse after reflection [see Fig. 3(a), black line].

To obtain the temporal profile of a probe pulse reflected off the inhomogeneous grating density, we first determine the spectrum of the reflected pulse $rp(\Delta) = I(\Delta)R(\Delta)\exp(i\Phi(\Delta))$, where $I(\Delta)$ is the spectrum of the incoming probe pulse. Taking the inverse Fourier transform of $rp(\Delta)$, we then obtain the temporal (and thus spatial) envelope of the reflected pulse. In Fig. 6, we compare the electric field of the reflected probe pulse of the PIC simulation [shown in Fig. 3(a)] with the envelope obtained via the coupled mode model (for the same parameters). Again, the coupled mode result is very close to the result of the PIC simulation.

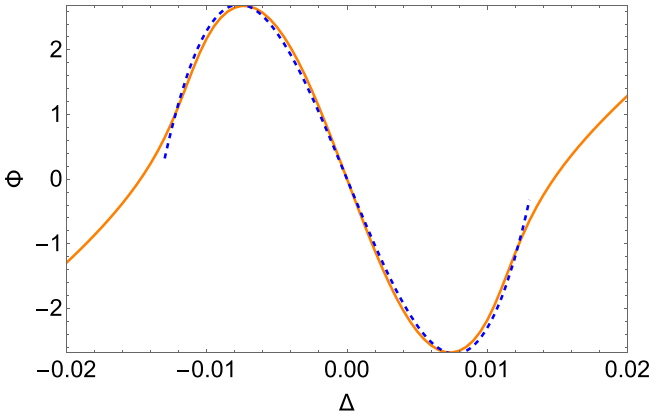

FIG. 5. Spectral phase $\Phi(\Delta)$ (solid orange line) and cubic polynomial fit (blue dashed line) for the same Δ region as in Fig. 4. The fit is only obtained in the region, where $R(\Delta)$ is nonvanishing.

C. Comparison with a quasihomogeneous case

To highlight the qualitative differences between inhomogeneous and homogeneous gratings, we compare the results obtained with those associated with homogeneous gratings. The question, of course, is which homogeneous gratings to compare with. We address this issue by increasing $\langle x^2\rangle$ while keeping all other parameters constant. If $\sqrt{\langle x^2\rangle}$ is significantly larger than the given length L, then the grating is effectively homogeneous. For a qualitative comparison, this constructive approach seems meaningful enough to us.

1. Side-lobe suppression

On completing the paper, we learned that an analogy to fiber gratings exists [87]. In that context, manufacturing methods are being discussed to photowrite Bragg gratings with grading (apodization) of the refractive index variation to approach zero at the end of the grating. Apodization of the refractive index change leads to side-lobe suppression in the

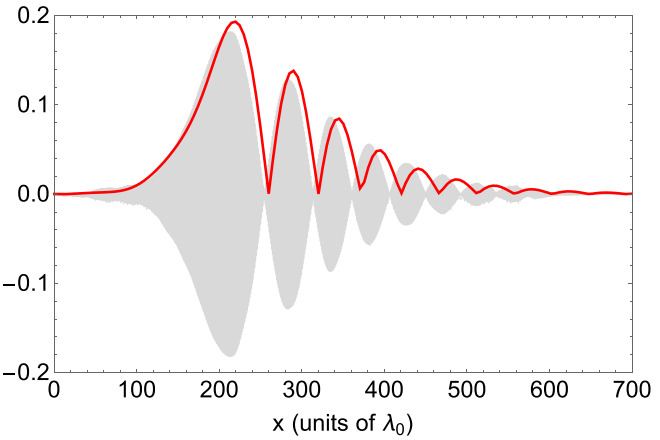

FIG. 6. Electric field of the 30 fs probe pulse reflected off the inhomogeneous plasma density grating in Fig. 3(a) as obtained in PIC simulation (light gray). The envelope of the electric field obtained from the coupled mode model for the same parameters is shown by the line [red (black)].

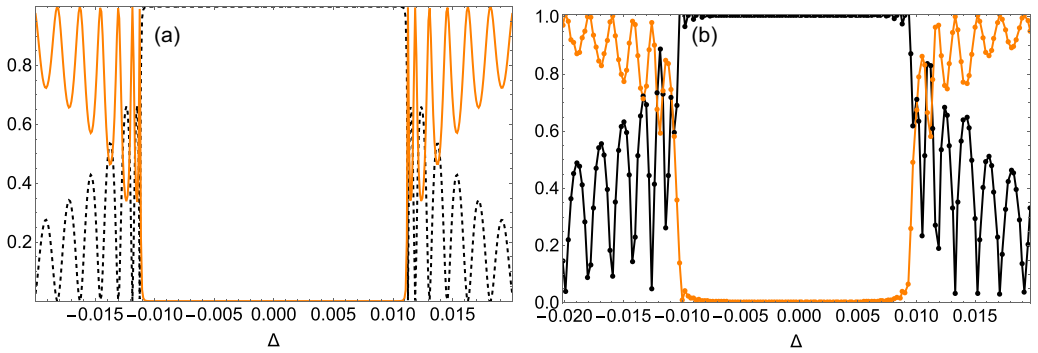

FIG. 7. (a) Solutions of the coupled mode equations for the transmission coefficient T [orange (light gray) solid line] and the reflection coefficient R (black line). The parameters are the same as in Fig. 4 except that $\langle x^2\rangle = 100\,000$ is now much larger. The grating is nearly homogeneous and we observe very pronounced side lobes. (b) Results for T and R obtained from a PIC simulation for the same parameters as (a).

transmission-reflection spectrum while maintaining reflectivity and a narrow bandwidth. As we shall demonstrate now, exactly the same happens in our present case.

In Fig. 7 we show results for reflection and transmission of a probe pulse propagating in an almost homogeneous grating. As mentioned already, homogeneity is established by changing $\langle x^2\rangle$ of the pump pulses from 2300 to 100 000. All other parameters are the same as in Sec. III. Clearly, side lobes appear. The reduction of side lobes is an important aspect in the design and optimization of signal processing systems [87]. So even though it was not evident from the beginning, the inhomogeneity in plasma gratings generated by narrower pump pulses is now proving to be an advantage.

2. *Third-order phase*

In Sec. III, we found a third-order phase that implies a quadratic chirp. To verify that this is indeed an inhomogeneity effect, we will examine the transition to the homogeneous situation. Figure 8 illustrates the important difference from the result in Sec. III when we take the homogeneous limit. Again, we compare the case $\langle x^2\rangle = 2300$ with $\langle x^2\rangle = 100\,000$. In the quasihomogeneous case, the phase is clearly linear as long as we are not in the immediate vicinity of the band edge.

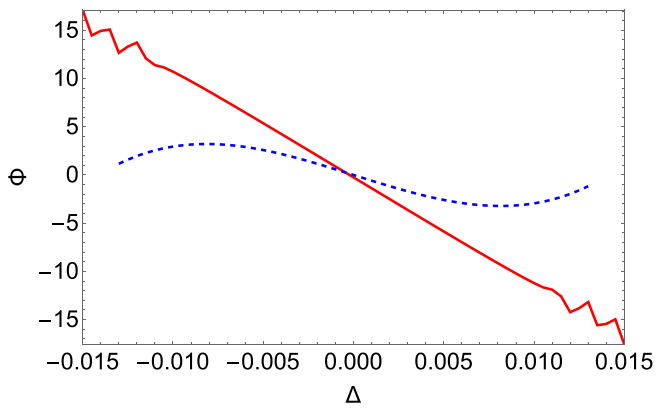

FIG. 8. Phase $\Phi = \arg(r)$ for the same parameters as in Fig. 7, i.e., in the quasihomogeneous case with $\langle x^2\rangle = 100\,000$ as obtained from the coupled mode equations. For comparison, the dashed line originates from the inhomogeneous case depicted in Fig. 5.

Third-order spectral phase, as it appears in the Gaussian grating of Sec. III, means a quadratic group delay versus frequency. When the central frequency of a pulse arrives first, the frequencies on either side arrive later. Two slightly different frequencies cause intensity beats as function of time. So, as appearing in the inhomogeneous case of Sec. III, the third-order spectral phase contribution causes oscillations after the main pulse. On the other hand, a linear spectral phase variation only corresponds to a shift in time (delay) of the whole pulse.

IV. SUMMARY AND OUTLOOK

When plasma gratings are produced by counterpropagating short laser pulses, generically the plasma grating is spatially inhomogeneous since it results from the superposition of the pump pulses envelopes. The effect of grating inhomogeneity on reflection, transmission, and chirp of a (reflected) probe pulse was studied in detail. Numerical PIC simulations were supported by theoretical analysis based on coupled mode equations as well as an effective medium approach.

At first, the generation of inhomogeneous plasma gratings was analyzed via PIC simulations for two finite-duration pump pulses undergoing head-on collision in a sufficiently long plasma slab. The resulting plasma density gratings are of fairly typical form. Over sufficient time, this form can be predicted by a simple fluid model. The model displays both the bottom-up asymmetry and deviations from simple harmonic behavior. For *analytical* discussions we use a simple harmonic approximation. Generalizations including higher harmonics are possible. The approximation for $M = 1$ provides very good agreement with the PIC simulations, not only qualitatively but also quantitatively. The reason for this good correspondence lies in the fact that only the $M = 1$ mode allows for an effective wave-number matching between the incident and reflected wave [45].

Next we investigated the propagation of a probe pulse interacting with the (inhomogeneous) plasma grating. Using PIC simulations, transmission and reflection were determined. Generically, we detected that the reflected pulse becomes chirped. The phase is of third order, which induces a quadratic chirp. In any case, in the Gaussian scenario, the side lobes in the frequency dependent reflection and transmission coefficients vanished, resulting in what we could interpret as an

optimization of the grating design. The reasons for the observed behavior could be uncovered through a simple coupled mode model.

Possible future applications of plasma density gratings such as mirrors, waveplates, polarizers, and possibly pulse compressors will need to be aware of the introduction of what will in most cases be a quadratic chirp to the reflected and transmitted pulses. This could deteriorate achievable pulse quality. On the other hand, the reduction of side lobes in the spectrum can increase pulse quality for certain applications.

In the Appendix, we supplemented the coupled mode analysis by an effective medium approach. The latter was quantified within a WKB analysis. The dual analytical modeling was conducted with the intention of providing various strategies for future investigations that lead to similar results. If a numerical solution of coupled differential equations proves to be too computationally intensive at the moment, then it becomes evident that the effective medium approach can be fruitful, although it may not capture all intricacies, such as spectrum side-lobe suppression, for instance.

It should be emphasized that both the coupled mode analysis and the effective mode approach can be readily generalized to other scenarios. Our particular focus lies on chirped plasma gratings, where we see substantial potential for applications. In particular, the generation of apodized plasma gratings with linear chirp will be of great practical significance. We intend to dedicate a separate paper to this specific area of research.

ACKNOWLEDGMENTS

Computational support and infrastructure was provided by the Centre for Information and Media Technology (ZIM) at the University of Düsseldorf (Germany). Development of the EPOCH PIC code used in this work was in part funded by the UK EPSRC Grants No. EP/G054950/1, No. EP/G056803/1, No. EP/G055165/1, and No. EP/M022463/1.

APPENDIX: EFFECTIVE MEDIUM APPROACH

We may also analyze part of the PIC results with the help of an effective medium approach. A comparison with the predictions from the coupled mode equations will be interesting.

First, in this Appendix, we set up the effective medium model. Subsequently, the model will be solved in WKB approximation for a quantitative evaluation of the transmission and reflection coefficients.

1. General outline

When introducing the combinations [77,78]

$$E^{\text{eff}} = u + v, \quad H^{\text{eff}} = u - v, \tag{A1}$$

$$\epsilon_{\text{eff}} = \sigma + \kappa, \quad \mu_{\text{eff}} = \sigma - \kappa, \tag{A2}$$

the coupled mode equations may be rewritten in

$$\frac{dE^{\text{eff}}}{dx} = i\,\mu_{\text{eff}}\,H^{\text{eff}}, \quad \frac{dH^{\text{eff}}}{dx} = i\,\epsilon_{\text{eff}}\,E^{\text{eff}}. \tag{A3}$$

We clearly recognize the analogy to Maxwell's equations for the propagation of an electromagnetic plane wave with unit frequency through a medium with dielectric permitivity $\epsilon_{\text{eff}}(x)$ and magnetic permeability $\mu_{\text{eff}}(x)$ [78]. This suggests introducing an effective refractive index,

$$N_{\text{eff}} = \sqrt{\epsilon_{\text{eff}} \cdot \mu_{\text{eff}}}. \tag{A4}$$

In case of homogeneous and infinite arrays, clearly imaginary N_{eff} forbid wave propagation (band gap) while for real N_{eff} waves could propagate.

Let us first study the general behavior before we focus on more specific details. We evaluate N_{eff} for the model (41) and (42), leading to

$$\epsilon_{\text{eff}} = \frac{2\pi}{N_0}\Delta + \frac{\pi N_0}{2}\left(1 - \frac{1}{N_0^2}\right)A(x), \tag{A5}$$

$$\mu_{\text{eff}} = \frac{2\pi}{N_0}\Delta - \frac{\pi N_0}{2}\left(1 - \frac{1}{N_0^2}\right)A(x), \tag{A6}$$

and

$$N_{\text{eff}}^2 \approx \frac{4\pi^2}{N_0^2}\Delta^2 - \frac{\pi^2 N_0^2}{4}\left(1 - \frac{1}{N_0^2}\right)^2 A^2(x), \quad A(x) = \alpha_1 e^{-\frac{x^2}{\langle x^2\rangle}}. \tag{A7}$$

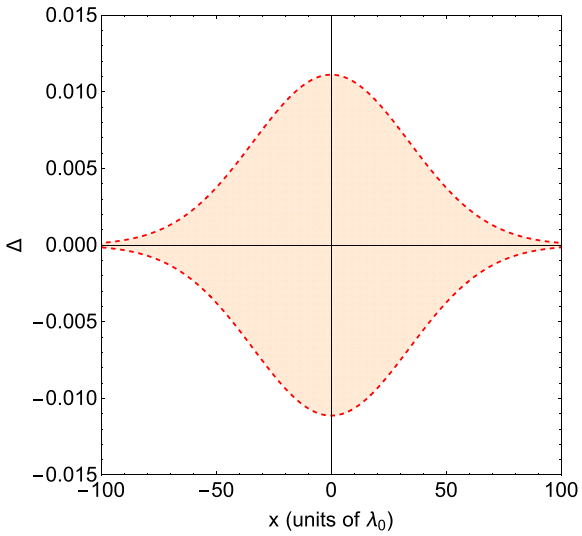

FIG. 9. Contour plot of the square of effective refractive index N_{eff}. In the shaded area $N_{\text{eff}}^2 \leqslant 0$. Parameters are $\langle x^2\rangle = 2300$, $\alpha_1 = 0.89$, and $n_0/n_c = 0.05$.

In Fig. 9 we present a contour plot of N_{eff}^2. We recognize different regions of behavior, depending on Δ and x. Within the shaded area $N_{\text{eff}}^2 \leqslant 0$. When a wave with fixed $\Delta > 0$ hits the grating from outside, the wave (which initially propagates freely) will decay in the shaded area. If the latter is finite, then the wave emerges weakened into the open (transmission) and is partially reflected.

2. WKB analysis

A discussion of the effective refractive index N_{eff} allows us to find the regions in ω for free wave propagation. In the other areas, a wave may tunnel through the forbidden area. To quantify the corresponding reflection and transmission properties, we use a phase-integral (WKB) method [78].

We assume that $\epsilon_{\rm eff}$ as well as $\mu_{\rm eff}$ are slowly varying in space. When introducing

$$\tilde{E}^{\rm eff} = \frac{1}{\sqrt{\mu_{\rm eff}}} E^{\rm eff}, \tag{A8}$$

$$\tilde{H}^{\rm eff} = \frac{1}{\sqrt{\epsilon_{\rm eff}}} H^{\rm eff}, \tag{A9}$$

we obtain for $\tilde{E}^{\rm eff}$ and $\tilde{H}^{\rm eff}$ second-order differential equations which for slowly varying $\epsilon_{\rm eff}$ and $\mu_{\rm eff}$ approximately reduce to

$$\frac{d^2\tilde{E}^{\rm eff}}{dx^2} + N_{\rm eff}^2(x)\,\tilde{E}^{\rm eff}(x) = 0, \tag{A10}$$

$$\frac{d^2\tilde{H}^{\rm eff}}{dx^2} + N_{\rm eff}^2(x)\,\tilde{H}^{\rm eff}(x) = 0. \tag{A11}$$

They have the standard Schrödinger form. Now we may follow the well-known procedure for phase-integral solutions. The WKB solutions lose their validity in the region close to $N_{\rm eff} = 0$, i.e., at turning points $x = x_1$ and $x = x_2 = -x_1$. For our simple model (29) with $M = 1$, the turning points are

$$x_{1,2} = \pm\sqrt{\langle x^2\rangle}\sqrt{-\ln\left[\frac{4|\Delta|}{(1-N_0^2)\alpha_1}\right]} \tag{A12}$$

in the Δ region

$$-\frac{\alpha_1}{4}\left(1-N_0^2\right) \leqslant \Delta \leqslant \frac{\alpha_1}{4}\left(1-N_0^2\right). \tag{A13}$$

The solutions at the different sides of the turning points will be connected by the WKB connection formulas.

Matrix $W(\theta)$, with

$$\theta = \int_{x_1}^{x_2} |N_{\rm eff}|\,dx \tag{A14}$$

integrated over the evanescent area $x_1 \leqslant x \leqslant x_2$, specifies the connection. Matrix P is defined as the propagation matrix for $N_{\rm eff}^2 > 0$, and Γ is the impedance matrix needed to relate the phase coefficients in the effective electric fields to the functions u and v, respectively. All the matrix definitions belong to the standard repertoire of quantum mechanics and will not be derived here in detail. An excellent summary is provided by Ref. [78].

Anticipating the explicit matrix forms as well as the connection formula provided by the reference [78], we finally obtain the result for u and v:

$$\begin{bmatrix} u(-L) \\ v(-L) \end{bmatrix} = \underbrace{\Gamma[\mathcal{Z}(-L)]\cdot P[\phi(-L)]\cdot W[\theta]\cdot P^{-1}[\phi(L)]\cdot\Gamma^{-1}[\mathcal{Z}(L)]}_{\mathcal{M}} \begin{bmatrix} u(L) \\ v(L) \end{bmatrix}. \tag{A15}$$

Here the phase factors are

$$\phi(-L) = \int_{-L}^{x_1} N_{\rm eff}\,dx, \quad \phi(L) = \int_{x_2}^{L} N_{\rm eff}\,dx, \tag{A16}$$

and the impedance $\mathcal{Z}$ should be determined from

$$\mathcal{Z}^2 = \frac{\mu_{\rm eff}(x)}{\epsilon_{\rm eff}(x)} \tag{A17}$$

at $x = \pm L$. The propagation matrix is

$$P(\phi) = \begin{pmatrix} e^{i\phi} & 0 \\ 0 & e^{-i\phi} \end{pmatrix}, \tag{A18}$$

where for ϕ the values $\phi(-L)$ and $\phi(L)$ have to be inserted.

The impedance matrix is

$$\Gamma(\mathcal{Z}) = \frac{\sqrt{|\mathcal{Z}|}}{2\mathcal{Z}}\begin{pmatrix} \mathcal{Z}+1 & \mathcal{Z}-1 \\ \mathcal{Z}-1 & \mathcal{Z}+1 \end{pmatrix}, \tag{A19}$$

where in our case [$\mu_{\rm eff}(\pm L) < 0$, $\epsilon_{\rm eff}(\pm L) < 0$ for $\Delta < 0$]

$$\mathcal{Z}(x) = -\sqrt{\mu_{\rm eff}(x)/\epsilon_{\rm eff}(x)}\,; \tag{A20}$$

it should be used and evaluated at $x = \pm L$.

Finally, the connection matrix is in our case [$\epsilon_{\rm eff}(x_1) = \epsilon_{\rm eff}(x_2) = 0$ for $\Delta < 0$]

$$W(\theta) = \begin{bmatrix} e^{\theta} + \frac{1}{4}e^{-\theta} & -i(e^{\theta} - \frac{i}{4}e^{-\theta}) \\ i(e^{\theta} - \frac{i}{4}e^{-\theta}) & e^{\theta} + \frac{1}{4}e^{-\theta} \end{bmatrix}. \tag{A21}$$

Most interesting for the present application is the fact that the elements of the matrix $\mathcal{M}$

$$\mathcal{M} = \begin{pmatrix} \frac{1}{t} & \frac{r^*}{t^*} \\ \frac{r}{t} & \frac{1}{t^*} \end{pmatrix} \tag{A22}$$

directly lead to the reflection coefficient $R = |r|^2$ and the transmission coefficient $T = |t|^2$. Thus, one easily can determine the transmission coefficient T and the reflection coefficient R. Some typical results are shown in Fig. 10. They

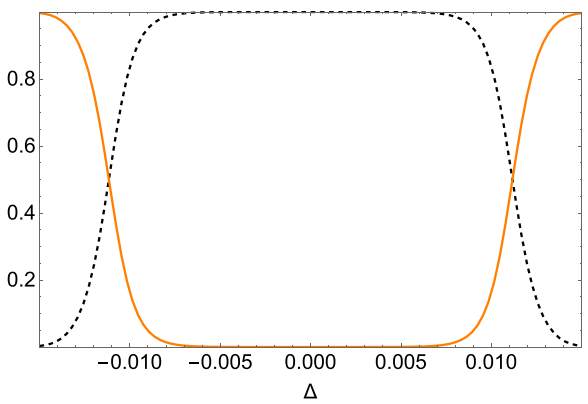

FIG. 10. Effective medium results for the transmission coefficient T [orange (light gray) solid line] and the reflection coefficient R (black dashed line) in the region $-0.015 \leqslant \Delta \leqslant 0.015$. The evaluation is for the same parameters as in Fig. 9.

approximate very well the results obtained by the coupled mode equations shown in Fig. 4.

Naturally, the WKB method implies limitations in the evaluation. It applies only to the shaded Δ region of Fig. 9. Outside, the effective medium approach predicts $R = 0$ and $T = 1$. We need well-defined turning points x_1 and x_2. As a result, we have restricted the evaluation in the figure to $-0.011 \leqslant \Delta \leqslant 0.011$. Nevertheless, the highly intuitive effective medium approach provides a very good agreement with the PIC results in the regions where the physically motivated analysis can be successful at all.

[1] P. Vukusic, Manipulating the flow of light with photonic crystals, Phys. Today **59**, 82 (2006).

[2] Caleb Q. Cook and Ariel Amir, Theory of chirped photonic crystals in biological broadband reflectors, Optica **3**, 1436 (2016).

[3] Ariel Amir and Peter Vukusic, Elucidating the stop bands of structurally colored systems through recursion, Am. J. Phys. **81**, 253 (2013).

[4] D. Strickland and G. Mourou, Compression of amplified chirped optical pulses, Opt. Commun. **55**, 447 (1985).

[5] Leonid Glebov, Vadim Smirnov, Eugeniu Rotari, Ion Cohanoschi, Larissa Glebova, Oleg Smolski, Julien Lumeau, Christopher Lantigua, and Alexei Glebov, Volume-chirped Bragg gratings: Monolithic components for stretching and compression of ultrashort laser pulses, Opt. Eng. **53**, 051514 (2014).

[6] V. M. Malkin and N. J. Fisch, Manipulating ultraintense laser pulses in plasmas, Phys. Plasmas **12**, 044507 (2005).

[7] H. Peng, J.-R. Marquès, L. Lancia, F. Amiranoff, R. L. Berger, S. Weber, and C. Riconda, Plasma optics in the context of high intensity lasers, Matter Radiat. Extr. **4**, 065401 (2019).

[8] Matthew R. Edwards, Nathaniel J. Fisch, and Julia M. Mikhailova, Laser-driven plasma sources of intense, ultrafast, and coherent radiation, Phys. Plasmas **28**, 013105 (2021).

[9] Y. Michine and H. Yoneda, Ultra high damage threshold optics for high power lasers, Commun. Phys. **3**, 24 (2020).

[10] P. Michel, *Plasma Photonics: Manipulating Light Using Plasmas*, Tech. Rep. LLNL-TR-818220 (Lawrence Livermore National Laboratory, Livermore, CA 2021).

[11] G. Shvets, N. J. Fisch, A. Pukhov, and J. Meyer-ter-Vehn, Superradiant amplification of an ultrashort laser pulse in a plasma by a counterpropagating pump, Phys. Rev. Lett. **81**, 4879 (1998).

[12] V. M. Malkin, G. Shvets, and N. J. Fisch, Fast compression of laser beams to highly overcritical powers, Phys. Rev. Lett. **82**, 4448 (1999).

[13] L. Lancia, A. Giribono, L. Vassura, M. Chiaramello, C. Riconda, S. Weber, A. Castan, A. Chatelain, A. Frank, T. Gangolf, M. N. Quinn, J. Fuchs, and J.-R. Marquès, Signatures of the self-similar regime of strongly coupled stimulated Brillouin scattering for efficient short laser pulse amplification, Phys. Rev. Lett. **116**, 075001 (2016).

[14] A. E. Hussein, J. Ludwig, K. Behm, Y. Horovitz, P.-E. Masson-Laborde, V. Chvykov, A. Maksimchuk, T. Matsuoka, C. McGuffey, V. Yanovsky, W. Rozmus, and K. Krushelnick, Stimulated Raman backscattering from a laser wakefield accelerator, New J. Phys. **20**, 073039 (2018).

[15] J.-R. Marquès, L. Lancia, T. Gangolf, M. Blecher, S. Bolanos, J. Fuchs, O. Willi, F. Amiranoff, R. L. Berger, M. Chiaramello, S. Weber, and C. Riconda, Joule-level high effiency energy transfer to sub-picosecond laser pulses by a plasma-based amplifier, Phys. Rev. X **9**, 021008 (2019).

[16] Z. Wu, Q. Chen, A. Morozov, and S. Suckewer, Compression of laser pulses by near-forward Raman amplification in plasma, Phys. Plasmas **27**, 013104 (2020).

[17] A. Frank, J. Fuchs, L. Lancia, G. Lehmann, J. Marques, G. Mourou, C. Riconda, K. H. Spatschek, T. Toncian, L. Vassura, S. Weber, and O. Willi, Amplification of ultra-short light pulses by ion collective modes in plasmas, Eur. Phys. J. Spec. Top. **223**, 1153 (2014).

[18] Matthew R. Edwards and Pierre Michel, Plasma transmission gratings for compression of high-intensity laser pulses, Phys. Rev. Appl. **18**, 024026 (2022).

[19] Zhaohui Wu, Yanlei Zuo, Xiaoming Zeng, Zhaoli Li, Zhimeng Zhang, Xiaodong Wang, Bilong Hu, Xiao Wang, Jie Mu, Jingqin Su, Qihua Zhu, and Yaping Dai, Laser compression via fast-extending plasma gratings, Matter Radiat. Extr. **7**, 064402 (2022).

[20] S. Monchocé, S. Kahaly, A. Leblanc, L. Videau, P. Combis, F. Réau, D. Garzella, P. D'Oliveira, Ph. Martin, and F. Quéré, Optically controlled solid-density transient plasma gratings, Phys. Rev. Lett. **112**, 145008 (2014).

[21] D. Turnbull, P. Michel, T. Chapman, E. Tubman, B. B. Pollock, C. Y. Chen, C. Goyon, J. S. Ross, L. Divol, N. Woolsey, and J. D. Moody, High power dynamic polarization control using plasma photonics, Phys. Rev. Lett. **116**, 205001 (2016).

[22] Kenan Qu, Qing Jia, and Nathaniel J. Fisch, Plasma q-plate for generation and manipulation of intense optical vortices, Phys. Rev. E **96**, 053207 (2017).

[23] David J. Stark, Chinmoy Bhattacharjee, Alexey V. Arefiev, Toma Toncian, R. D. Hazeltine, and S. M. Mahajan, Relativistic plasma polarizer: Impact of temperature anisotropy on relativistic transparency, Phys. Rev. Lett. **115**, 025002 (2015).

[24] D. Turnbull, C. Goyon, G. E. Kemp, B. B. Pollock, D. Mariscal, L. Divol, J. S. Ross, S. Patankar, J. D. Moody, and P. Michel, Refractive index seen by a probe beam interacting with a laser-plasma system, Phys. Rev. Lett. **118**, 015001 (2017).

[25] G. Lehmann and K. H. Spatschek, Plasma-based polarizer and waveplate at large laser intensity, Phys. Rev. E **97**, 063201 (2018).

[26] L.-L. Yu, Y. Zhao, L.-J. Qian, M. Chen, S.-M. Weng, Z.-M. Sheng, D. A. Jaroszynski, W. B. Mori, and J. Zhang, Plasma optical modulators for intense lasers, Nat. Commun. **7**, 11839 (2016).

[27] R. Pompili, M. P. Anania, M. Bellaveglia, A. Biagioni, S. Bini, F. Bisesto, E. Brentegani, F. Cardelli, G. Castorina, E. Chiadroni, A. Cianchi, O. Coiro, G. Costa, M. Croia, D. Di Giovenale, M. Ferrario, F. Filippi, A. Giribono, V. Lollo, A. Marocchino, M. Marongiu, V. Martinelli, A. Mostacci, D. Pellegrini, L. Piersanti, G. Di Pirro, S. Romeo, A. R. Rossi,

J. Scifo, V. Shpakov, A. Stella, C. Vaccarezza, F. Villa, and A. Zigler, Focusing of high-brightness electron beams with active-plasma lenses, Phys. Rev. Lett. **121**, 174801 (2018).

[28] C. A. Lindstrøm, E. Adli, G. Boyle, R. Corsini, A. E. Dyson, W. Farabolini, S. M. Hooker, M. Meisel, J. Osterhoff, J.-H. Röckemann, L. Schaper, and K. N. Sjobak, Emittance preservation in an aberration-free active plasma lens, Phys. Rev. Lett. **121**, 194801 (2018).

[29] M. Nakatsutsumi, A. Kon, S. Buffechoux, P. Audebert, J. Fuchs, and R. Kodama, Fast focusing of short-pulse lasers by innovative plasma optics toward extreme intensity, Opt. Lett. **35**, 2314 (2010).

[30] Ming Zeng, Alberto Martinez de la Ossa, Kristjan Poder, and Jens Osterhoff, Plasma lenses for relativistic laser beams in laser wakefield accelerators, Phys. Plasmas **27**, 023109 (2020).

[31] I. Y. Dodin and N. J. Fisch, Storing, retrieving, and proprocess optical information by Raman backscattering in plasmas, Phys. Rev. Lett. **88**, 165001 (2002).

[32] I. Y. Dodin and N. J. Fisch, Dynamic volume holography and optical information processing by Raman scattering, Opt. Commun. **214**, 83 (2002).

[33] G. Lehmann and K. H. Spatschek, Plasma volume holograms for focusing and mode conversion of ultraintense laser pulses, Phys. Rev. E **100**, 033205 (2019).

[34] M. R. Edwards, V. R. Munirov, A. Singh, N. M. Fasano, E. Kur, N. Lemos, J. M. Mikhailova, J. S. Wurtele, and P. Michel, Holographic plasma lenses, Phys. Rev. Lett. **128**, 065003 (2022).

[35] G. Lehmann and K. H. Spatschek, Wakefield stimulated terahertz radiation from a plasma grating, Plasma Phys. Control. Fusion **64**, 034001 (2022).

[36] R. K. Kirkwood, D. P. Turnbull, T. Chapman, S. C. Wilks, M. D. Rosen, R. A. London, L. A. Pickworth, W. H. Dunlop, J. D. Moody, D. J. Strozzi, P. A. Michel, L. Divol, O. L. Landen, B. J. MacGowan, B. M. Van Wonterghem, K. B. Fournier, and B. E. Blue, Plasma-based beam combiner for very high fluence and energy, Nat. Phys. **14**, 80 (2018).

[37] Z.-M. Sheng, J. Zhang, and D. Umstadter, Plasma density gratings induced by intersecting laser pulses in underdense plasmas, Appl. Phys. B **77**, 673 (2003).

[38] P. Michel, L. Divol, E. A. Williams, S. Weber, C. A. Thomas, D. A. Callahan, S. W. Haan, J. D. Salmonson, S. Dixit, D. E. Hinkel, M. J. Edwards, B. J. MacGowan, J. D. Lindl, S. H. Glenzer, and L. J. Suter, Tuning the implosion symmetry of iCF targets via controlled crossed-beam energy transfer, Phys. Rev. Lett. **102**, 025004 (2009).

[39] P. Michel, L. Divol, D. Turnbull, and J. D. Moody, Dynamic control of the polarization of intense laser beams via optical wave mixing in plasmas, Phys. Rev. Lett. **113**, 205001 (2014).

[40] G. Lehmann and K. H. Spatschek, Transient plasma photonic crystal for high-power lasers, Phys. Rev. Lett. **116**, 225002 (2016).

[41] H. Peng, C. Riconda, M. Grech, J.-Q. Su, and S. Weber, Nonlinear dynamics of laser-generated ion-plasma gratings: A unified description, Phys. Rev. E **100**, 061201(R) (2019).

[42] S. E. Schrauth, A. Colaitis, R. L. Luthi, R. C. W. Plummer, W. G. Hollingsworth, C. W. Carr, M. A. Norton, R. J. Wallace, A. V. Hamza, B. J. MacGowan, M. J. Shaw, M. L. Spaeth, K. R. Manes, P. Michel, and J.-M. Di Nicola, Study of self-diffraction from laser generated plasma gratings in the nanosecond regime, Phys. Plasmas **26**, 073108 (2019).

[43] H. Peng, C. Riconda, M. Grech, C.-T. Zhou, and S. Weber, Dynamical aspects of plasma gratings driven by a static ponderomotive potential, Plasma Phys. Control. Fusion **62**, 115015 (2020).

[44] A. V. Andreev, A. V. Balakin, I. A. Ozheredov, A. P. Shkurinov, P. Masselin, G. Mouret, and D. Boucher, Compression of femtosecond laser pulses in thin one-dimensional photonic crystals, Phys. Rev. E **63**, 016602 (2000).

[45] Amnon Yariv and Pochi Yeh, *Optical Waves in Crystals* (Wiley Interscience, New York, 2002).

[46] Pochi Yeh, *Optical Waves in Layered Media* (Wiley Intersience, New York, 2005).

[47] H.-C. Wu, Z.-M. Sheng, Q.-J. Zhang, Y. Cang, and J. Zhang, Controlling ultrashort intense laser pulses by plasma Bragg gratings with ultrahigh damage threshold, Laser Part. Beams **23**, 417 (2005).

[48] S. Suntsov, D. Abdollahpour, D. G. Papazoglou, and S. Tzortzakis, Femtosecond laser induced plasma diffraction gratings in air as photonic devices for high intensity laser applications, Appl. Phys. Lett. **94**, 251104 (2009).

[49] H. Y. Chen, Y. Yin, C. L. Tian, H. Xu, Y. Y. Ma, H. B. Zhuo, and F. Q. Shao, Moving electron density gratings induced in the beat-wave field of two counterpropagating laser pulses, Phys. Plasmas **17**, 083112 (2010).

[50] Magali Durand, Yi Liu, Benjamin Forestier, Aurélien Houard, and André Mysyrowicz, Experimental observation of a traveling plasma grating formed by two crossing filaments in gases, Appl. Phys. Lett. **98**, 121110 (2011).

[51] S. Hocquet, J. Neauport, and N. Bonod, Recent progress in the development of pulse compression gratings, EPJ Web Conf. **59**, 07002 (2013).

[52] A. Jarnac, M. Durand, A. Houard, Y. Liu, B. Prade, M. Richardson, and A. Mysyrowicz, Spatiotemporal cleaning of a femtosecond laser pulse through interaction with counterpropagating filaments in air, Phys. Rev. A **89**, 023844 (2014).

[53] Qing Jia, Ido Barth, M. R. Edwards, J. M. Mikhailova, and N. J. Fisch, Distinguishing Raman from strongly coupled Brillouin amplification for short pulses, Phys. Plasmas **23**, 053118 (2016).

[54] G. Lehmann and K. H. Spatschek, Laser-driven plasma photonic crystals for high-power lasers, Phys. Plasmas **24**, 056701 (2017).

[55] Y. Shi, J. Vieira, R. M. G. M. Trines, R. Bingham, B. F. Shen, and R. J. Kingham, Magnetic field generation in plasma waves driven by copropagating intense twisted lasers, Phys. Rev. Lett. **121**, 145002 (2018).

[56] G. Lehmann and K. H. Spatschek, Plasma photonic crystal growth in the trapping regime, Phys. Plasmas **26**, 013106 (2019).

[57] Joseph R. Smith, Chris Orban, Gregory K. Ngirmang, John T. Morrison, Kevin M. George, Enam A. Chowdhury, and W. M. Roquemore, Particle-in-cell simulations of density peak formation and ion heating from short pulse laser-driven ponderomotive steepening, Phys. Plasmas **26**, 123103 (2019).

[58] H. Ma, Su-Ming Weng, P. Li, X. Li, Y. Wang, S. Yew, Min Chen, Paul McKenna, and Z. Sheng, Growth, saturation and breaking down of laser-driven plasma density gratings, Phys. Plasmas **27**, 073105 (2020).

[59] G. Lehmann and K. H. Spatschek, Reflection and transmission properties of a finite-length electron plasma grating, Matter Radiat. Extr. **7**, 054402 (2022).

[60] G. K. Holt, G. Vieux, B. B. Ersfeld, S. R. Yoffe, A. Maitrallain, M. Shahzad, A. Kornaszewski, J. M. Dias, S. Krishnamurthy, D. R. Symes, N. Bourgeois, and D. A. Jaroszynski, Investigation of transient plasma photoniccrystals, in *Proceedings of the 47th EPS Conference on Plasma Physics* (European Physical Society (EPS), Mulhouse, 2021).

[61] George K. Holt, Gregory Vieux, Bernhard Ersfeld, Samuel R. Yoffe, James Feehan, Enrico Brunetti, Min Sup Hur, and Dino A. Jaroszynski, Investigations into the volume plasma density grating waveplate, in *Relativistic Plasma Waves and Particle Beams as Coherent and Incoherent Radiation Sources IV*, edited by Dino A. Jaroszynski and Min Sup Hur (SPIE, Bellingham, WA, 2021).

[62] Hui-Chun Wu, Zheng-Ming Sheng, Qiu-Ju Zhang, Yu Cang, and Jie Zhang, Manipulating ultrashort intense laser pulses by plasma Bragg gratings, Phys. Plasmas **12**, 113103 (2005).

[63] P. Michel, E. Kur, M. Lazarow, T. Chapman, L. Divol, and J. S. Wurtele, Polarization-dependent theory of two-wave mixing in nonlinear media, and application to dynamical polarization control, Phys. Rev. X **10**, 021039 (2020).

[64] Weidong Zhang, Haitao Wang, Xiaolin Zhao, and Weixia Lan, Bandgap-tunable device realized by ternary plasma photonic crystals arrays, Phys. Plasmas **27**, 063508 (2020).

[65] Jia Liu, Wenxue Li, Haifeng Pan, and Heping Zeng, Two-dimensional plasma grating by non-collinear femtosecond filament interaction in air, Appl. Phys. Lett. **99**, 151105 (2011).

[66] Ken Xingze Wang, Zongfu Yu, Victor Liu, Aaswath Raman, Yi Cui, and Shanhui Fan, Light trapping in photonic crystals, Energy Environ. Sci. **7**, 2725 (2014).

[67] Nicolas Bonod and Jérôme Neauport, Diffraction gratings: from principles to applications in high-intensity lasers, Adv. Opt. Photon. **8**, 156 (2016).

[68] Hui-Chu Wu, Zheng-Ming Sheng, and Jie Zhang, Chirped pulse compression in nonuniform plasma Bragg gratings, Appl. Phys. Lett. **87**, 201502 (2005).

[69] A. H. Gevorgyan, N. A. Vanyushkin, and M. S. Rafayelyan, Light localization in 1d chirped photonic crystals, Eur. Phys. J. Plus **137**, 719 (2022).

[70] S. Mokhov, Transmitting volume Bragg grating with longitudinal Moiré apodization, OSA Contin. **2**, 3471 (2019).

[71] S. Kaim, S. Mokhov, B. Y. Zeldovich, and L. B. Glebov, Stretching and compressing of short laser pulses by chirped Bragg gratings: analytic and numerical modeling, Opt. Eng. **53**, 05150 (2014).

[72] O. V. Belai, E. V. Podivilov, and D. A. Shapiro, Group delay in Bragg grating with linear chirp, Opt. Commun. **266**, 512 (2006).

[73] Zhenhua Tian and Lingyu Yu, Rainbow trapping of ultrasonic guided waves in chirped phononic crystal plates, Sci. Rep. **7**, 1 (2017).

[74] M. Sumetsky, B. J. Eggleton, and C. M. deSterke, Theory of group delay ripple generated by chirped fiber gratings, Opt. Express **10**, 332 (2002).

[75] Zhuang Rongrong and Cai Ping, Analysis on the reflection characteristic and the dispersion compensation performance of linear chirped fiber grating, Inf. Technol. J. **13**, 1868 (2014).

[76] R. Szipöcs, K. Ferencz, Chr. Spielmannn, and F. Krausz, Chirped multilayer coatings for broadband dispersion control in femtosecond lasers, Opt. Lett. **19**, 201 (1994).

[77] J. E. Sipe, L. Poladian, and M. deSterke, Propagation through nonuniform grating structures, J. Opt. Soc. Am. A **11**, 1307 (1994).

[78] L. Poladian, Graphical and WKB analysis of nonuniform Bragg gratings, Phys. Rev. E **48**, 4758 (1993).

[79] Igor V. Ciapurin, Leonid B. Glebov, and Vadim I. Smirnov, Modeling of Gaussian beam diffraction on volume Bragg gratings in PTR glass, in *Practical Holography XIX: Materials and Applications*, edited by Tung H. Jeong and Hans I. Bjelkhagen (SPIE, Bellingham, WA, 2005).

[80] C. Goyon, M.R. Edwards, T. Chapman, L. Divol, N. Lemos, G. J. Williams, D. A. Mariscal, D. Turnbull, A. M. Hansen, and P. Michel, Slow and fast light in plasma using optical wave mixing, Phys. Rev. Lett. **126**, 205001 (2021).

[81] A. M. Hansen, K. L. Nguyen, D. Turnbull, B. J. Albright, R. K. Follett, R. Huff, J. Katz, D. Mastrosimone, A. L. Milder, L. Yin, J. P. Palastro, and D. H. Froula, Cross-beam energy transfer saturation: Ion heating and pump depletion, Plasma Phys. Control. Fusion **64**, 034003 (2022).

[82] R. E. Slusher and B. J. Eggleton, eds., *Nonlinear Photonic Crystals*, Springer Series in Photonics, Vol. 10 (Springer, Berlin, 2003).

[83] H. J. Eichler, P. Günter, and D. W. Pohl, *Laser-induced Dynamic Gratings* (Springer, Berlin, 1986).

[84] https://cfsa-pmw.warwick.ac.uk/mediawiki/index.php/EPOCH:MainPage.

[85] H. Peng, C. Riconda, S. Weber, C. T. Zhou, and S. C. Ruan, Frequency conversion of lasers in a dynamic plasma grating, Phys. Rev. Appl. **15**, 054053 (2021).

[86] Rick Trebino, *Frequency-Resolved Optical Gating: The Measurement of Ultrashort Laser Pulses* (Springer, Berlin, 2000).

[87] Raman Kashyap, Apodization of fiber gratings, in *Fiber Bragg Gratings (Second Edition)*, edited by Raman Kashyap (Academic Press, Boston, 2010), pp. 189–215.